

Lithium niobate piezo-optomechanical crystals: supplementary material

WENTAO JIANG, RISHI N. PATEL, FELIX M. MAYOR, TIMOTHY P. MCKENNA, PATRICIO ARRANGOIZ-ARRIOLA, CHRISTOPHER J. SARABALIS, JEREMY D. WITMER, RAPHAËL VAN LAER, AND AMIR H. SAFAVI-NAEINI

Department of Applied Physics and Ginzton Laboratory, Stanford University, 348 Via Pueblo Mall, Stanford, California 94305, USA

Published 2 July 2019

This document provides supplementary information to “Lithium niobate piezo-optomechanical crystals,” <https://doi.org/10.1364/optica.6.000845>.

1. ORIENTATION DEPENDENCY OF OMC PROPERTIES

A. Definition of coordinate systems and rotated dielectric and photoelastic tensor

We start by defining the coordinate systems. The global coordinate system is fixed with the nanobeam with axis labeled by x, y, z , and the material coordinate system coincides with the crystal axis of LN, denoted by X, Y, Z . Note that for Euler angles which rotate the axis of the global coordinate system to the material coordinate system, the corresponding rotation matrix can be applied to transform the tensor components in the material system to the global system.

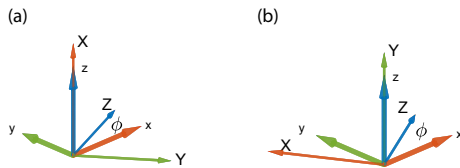


Fig. S1. Definition of the coordinate systems for (a) X-cut LN and (b) Y-cut LN. The global coordinate system is shown with thicker and shorter arrows, labeled with x, y, z . The material coordinate systems are shown with thinner and longer arrows, labeled with X, Y, Z . The nanobeam is parallel to the global x axis. The in-plane rotation angle ϕ is defined as the angle between x and Z axis in both case.

We first give the rotation matrix used for X-cut LN (LNX) and

Y-cut LN (LNY) with in-plane rotation angle ϕ as

$$R_{\text{LNX}}(\phi) = \begin{bmatrix} 0 & \sin \phi & \cos \phi \\ 0 & -\cos \phi & \sin \phi \\ 1 & 0 & 0 \end{bmatrix}, \quad (\text{S1})$$

$$R_{\text{LNY}}(\phi) = \begin{bmatrix} -\sin \phi & 0 & \cos \phi \\ \cos \phi & 0 & \sin \phi \\ 0 & 1 & 0 \end{bmatrix}. \quad (\text{S2})$$

The global coordinate system and the rotated material systems are shown in fig. S1. The corresponding Euler angles in ‘z-x-z’ convention are $(\alpha, \beta, \gamma) = (\phi - \pi/2, -\pi/2, -\pi/2)$ for LNX and $(\alpha, \beta, \gamma) = (\phi - \pi/2, -\pi/2, \pi)$ for LNY.

The photoelastic tensor components of the rotated crystal in the global coordinate system are then given by

$$p'_{ijkl}(\phi) = R_{im}(\phi)R_{jn}(\phi)R_{kp}(\phi)R_{lq}(\phi)p_{mnpq}. \quad (\text{S3})$$

Repeated indices are to be summed. The components of the rotated photoelastic tensor in the global coordinate system are given in Sec. 6.

For both LNX and LNY, the rotated dielectric tensor is

$$\epsilon' = \begin{bmatrix} \epsilon_{11} + \Delta\epsilon_{e0} \cos^2 \phi & \cos \phi \sin \phi \Delta\epsilon_{e0} & 0 \\ \cos \phi \sin \phi \Delta\epsilon_{e0} & \epsilon_{11} + \Delta\epsilon_{e0} \sin^2 \phi & 0 \\ 0 & 0 & \epsilon_{11} \end{bmatrix}, \quad (\text{S4})$$

where $\Delta\epsilon_{e0} = \epsilon_{33} - \epsilon_{11}$.

B. Simulation of optomechanical coupling rate

With the rotated dielectric and photoelastic tensor components, the photoelastic contribution of the optomechanical coupling is given by [S1]

$$g_{0,PE} = -\frac{\omega_c}{2} \frac{\int \mathbf{E} \cdot \frac{\partial \epsilon}{\partial \alpha} \cdot \mathbf{E} dV}{\int \mathbf{E} \cdot \mathbf{D} dV}, \quad (\text{S5})$$

where α parametrizes the mechanical motion amplitude, and $\partial \epsilon_{ij} / \partial \alpha = -\epsilon_{ik} \epsilon_{lj} p_{klmn} S_{mn} / \epsilon_0$. For isotropic media with refractive index n , the photoelastic induced change in dielectric constant simplifies to $\partial \epsilon_{ij} / \partial \alpha = -\epsilon_0 n^4 p_{ijmn} S_{mn}$.

Consider the qualitative dependence of photoelastic contribution to the optomechanical coupling rate g_0 . For breathing mechanical modes, the dominating strain component is S_{yy} in the global coordinate system. Similarly, for TE optical modes, the primary electric field component is E_y . As a result, the largest photoelastic contribution to g_0 is from $E_y^2 \partial \epsilon_{yy} / \partial \alpha \approx -\epsilon_0 n^4 p'_{22} S_{yy} E_y^2$. This suggests that we focus on the p'_{22} component of the rotated crystal in the global coordinate system.

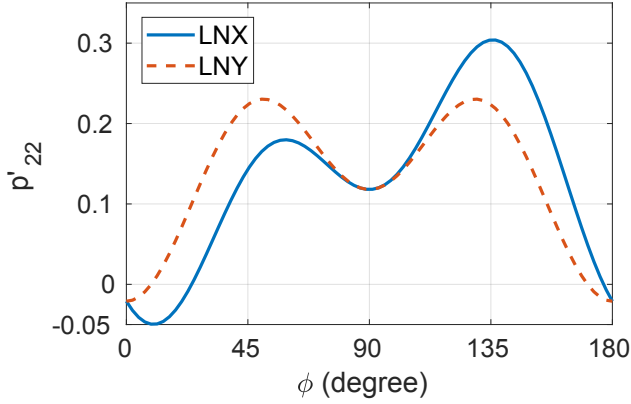


Fig. S2. Rotated photoelastic tensor component p'_{22} for LNX (solid blue) and LNY (dashed red).

We use photoelastic components from Ref. [S2] for numerical evaluations. The p'_{22} component of LNX and LNY is plotted in fig. S2. The maximal p'_{22} can be achieved on LNX with $\phi = 135$ degree, where $p'_{22} = (p_{11} + p_{33} + p_{13} + p_{31})/4 + p_{44} - (p_{14} + p_{41})/2 \approx 0.3$.

For the moving boundary contribution of the optomechanical interaction, we approximate LN as an isotropic dielectric material with refractive index $n = \sqrt{\epsilon_{LN}} = 2.2$. The contribution from moving boundary is [S1]

$$g_{0,MB} = -\frac{\omega_c}{2} \frac{\oint (\mathbf{Q} \cdot \mathbf{n})(\Delta \epsilon E_{\parallel}^2 - \Delta \epsilon^{-1} D_{\perp}^2) dS}{\int \mathbf{E} \cdot \mathbf{D} dV}, \quad (\text{S6})$$

where $\Delta \epsilon \equiv \epsilon_{LN} - \epsilon_{\text{air}}$, $\Delta \epsilon^{-1} \equiv \epsilon_{LN}^{-1} - \epsilon_{\text{air}}^{-1}$, \mathbf{Q} is the normalized displacement field and \mathbf{n} is the surface norm pointing towards the air. The subscripts \parallel and \perp denote the parallel and perpendicular component of the fields locally with respect to the surface.

We assume same mode profiles for different ϕ as a first-order approximation to calculate the ϕ -dependence of the optomechanical coupling rate g_0 . We evaluate eq. S5 and eq. S6 for different ϕ . In fig. S3 we show the photoelastic contribution $g_{0,PE}$ (dashed red), moving boundary contribution $g_{0,MB}$ (dashed dotted yellow) and the absolute values of the total g_0 (blue). From fig. S2,

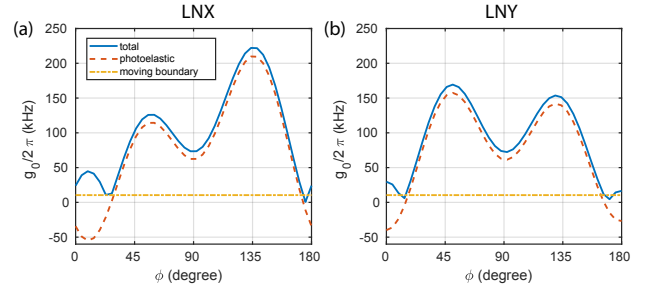


Fig. S3. Simulation of optomechanical coupling rate g_0 on (a) X-cut and (b) Y-cut LN for different in-plane rotation angle ϕ .

it is clear that p'_{22} is a good indicator of the optomechanical coupling rate.

C. Measurements of optical quality factors and optomechanical coupling rates with various ϕ

We fabricated OMCs on both LNX and LNY with various values of ϕ . The measured optical quality factors are shown in fig. S4(a, b). No obvious dependence of quality factors on ϕ is observed. The quality factors on LNY are generally lower due to fabrication variations between different chips. The mechanical quality factors at room temperature are typically $Q_m \sim 4000$. The room-temperature Q_m is limited by thermoelastic damping and is relatively insensitive to crystal orientations. At cryogenic temperature, the highest mechanical $Q_m = 37,000$ is observed on the LNY OMC with $\phi = 0$, where the y-symmetry of the nanobeam is recovered.

In fig. S4(c, d) we show the measured optomechanical coupling rates g_0 versus OMC orientation angle ϕ . The coupling rates were measured at room temperature (300 K) using calibrated thermal mechanical noise power spectral density [S3]. The measured g_0 's are in general roughly smaller than the simulated values by $\sim 50\%$. We attribute this discrepancy to the approximation of mode profiles, the fact that the design is only optimized for $\phi = 0$ on LNY, the possible differences in the material properties between simulation and the actual LNOS wafers, and the considerable uncertainties of LN's photoelastic components [S2].

Despite the discrepancy between the absolute values of the simulated and measured g_0 , we observe that the maximal optomechanical coupling rate occurs at $\phi = 135^\circ$ on LNX, agreeing with the simulations (fig. S3(a)) and also the simple prediction from p'_{22} (fig. S2). The optimal orientations on LNY are near $\phi = 45^\circ$ and $\phi = 135^\circ$, reasonably matching the simulation results in fig. S3(b).

2. THERMAL-OPTICAL SHIFT AND THERMAL RELAXATION

A. Thermal-optical shift

We observed a thermal-induced optical shift when scanning the laser over the optical cavity with different powers. The thermal-induced optical shift is well understood in silicon microcavities [S4]. To better understand the thermal-optical shift on LN OMC, we briefly describe the silicon case here.

In silicon microcavities, the heat absorption rate is proportional to the intracavity photon number n_c , leading to a local temperature change proportional to n_c . The temperature change affects the optical mode via thermal expansion and temperature-dependent refractive index change, both result in a wavelength

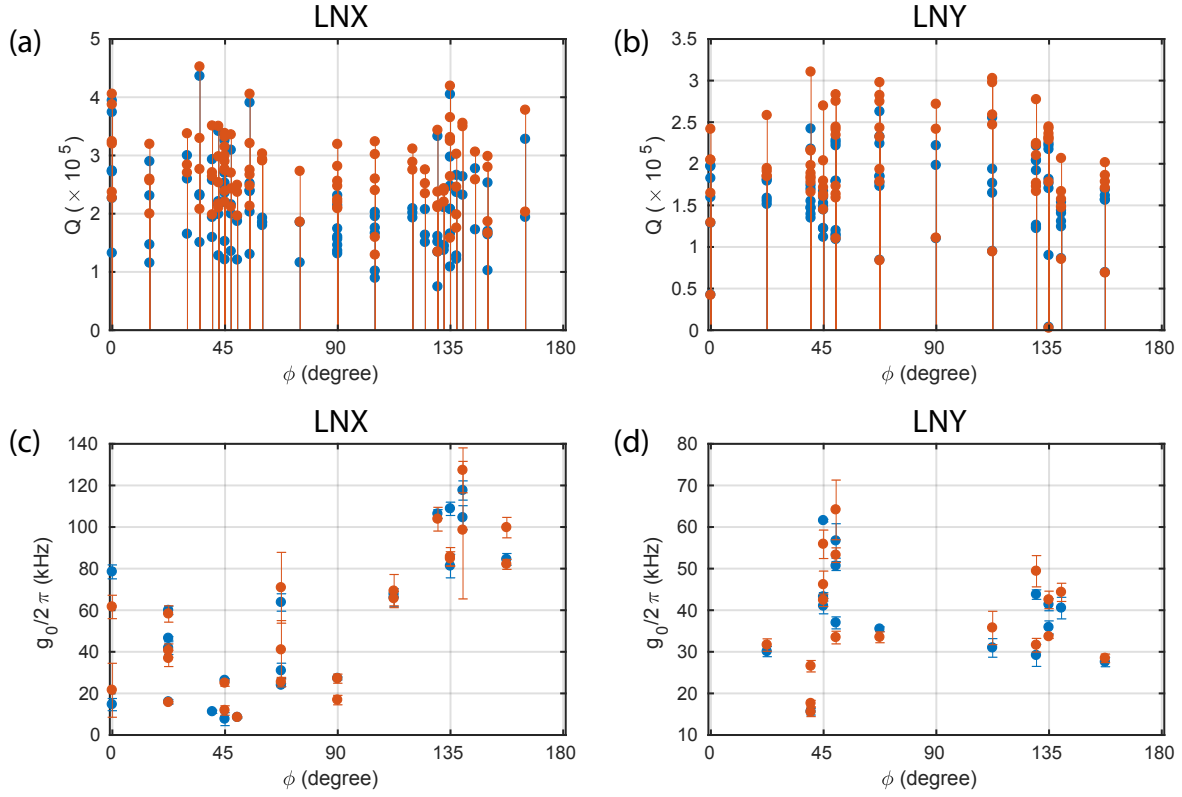


Fig. S4. Optical quality factor Q and optomechanical coupling rate g_0 on LNX and LNY. (a, b) Measured total (blue) and intrinsic (red) optical quality factors on LNX (a) and LNY (b). No obvious dependency on in-plane rotation ϕ can be observed. The quality factors on LNY are generally lower due to fabrication variations between different chips. (c, d) Measured zero-point optomechanical coupling rate g_0 for different ϕ on LNX (c) and LNY (d). Blue (red) data points represent measurement with detuning $\Delta = -\omega_m$ ($\Delta = \omega_m$). Error bars represent one standard deviation obtained by repeated measurements with different laser pump power.

shift that's linear with respect to the temperature change. A positive wavelength shift is usually observed for an increase in temperature. When the laser frequency approaches the optical cavity from the blue side, n_c , the temperature increase, and the optical cavity shifts red. When the laser reaches beyond the maximum wavelength shift which occurs for maximum n_c at the reflection dip, n_c starts decreasing. The cavity shifts back towards the blue side as a result of decreasing n_c , which further decreases n_c . This causes the cavity to jump back to nearly its original wavelength. The cavity red shift reflects itself in the continuous blue-to-red laser wavelength sweep as a slow slope which gets flatter for higher power. The mode escapes after the laser has passed the maximum shifted wavelength, giving a sharp jump in the transmission or reflection spectrum similar to Fig S5(a).

The thermal-induced optical shift $\Delta\lambda$ we observed on the LN OMC is qualitatively similar to silicon, but the wavelength shifts faster than linear and could be as large as few nanometers at high laser powers. As shown in fig. S5(a), the reflections were measured for linearly increasing laser scan powers, vertically displaced for viewing purposes. We extract the maximum wavelength shifts $\Delta\lambda_{\max}$ (fig. S5(b)) as well as minimum reflections at the resonance dip T_0 versus laser powers (fig. S5(c)). A sharp transition occurs near a threshold laser power $P_{\text{in, thres}} = 0.065$ mW. The wavelength shifts slow down and the transition dips get shallower.

With the coherent spectroscopy method, we confirmed that with powers $P_{\text{in}} > P_{\text{in, thres}}$ and n_c as high as 1.5×10^5 , the cavity linewidth stays roughly constant regardless of the increasing T_0 (see sec. 3). Little additional loss is introduced by the high optical powers used in our measurements. We conclude that the increase in T_0 is due to an “early escape” of the mode, where $\Delta\lambda$ saturates and the cavity escapes back to far blue before the laser reaches the reflection dip. Based on measurements of the reflection dip $T_0 = |(i\Delta + \kappa/2 - \kappa_e)/(i\Delta + \kappa/2)|^2$, we could obtain the detuning Δ right before the mode escapes and calculate the corresponding intracavity photon number n_c . This n_c is the maximal intracavity photon number obtained for each laser power. The results are shown in fig. S5(d). For laser powers below $P_{\text{in, thres}}$, the maximal n_c grows linearly with respect to input powers. When n_c reaches $n_{c, \text{thres}} \sim 1.4 \times 10^5$ at $P_{\text{in}} = P_{\text{in, thres}}$, the intracavity photon numbers are observed to saturate at values near $n_{c, \text{thres}}$, largely deviating from the linear relation (red line) regardless of increasing laser powers. Similar threshold behaviors in terms of n_c were observed on different OMC devices and showed no obvious correlation with the optical quality factors. The physical mechanism leading to the threshold and the dependence of $n_{c, \text{thres}}$ on system parameters are not understood and will be the subject of further exploration.

For n_c smaller than the threshold, we plot the wavelength shifts versus the intracavity photon numbers before $n_{c, \text{thres}}$ in fig. S5(e). A quadratic relationship between wavelength shift

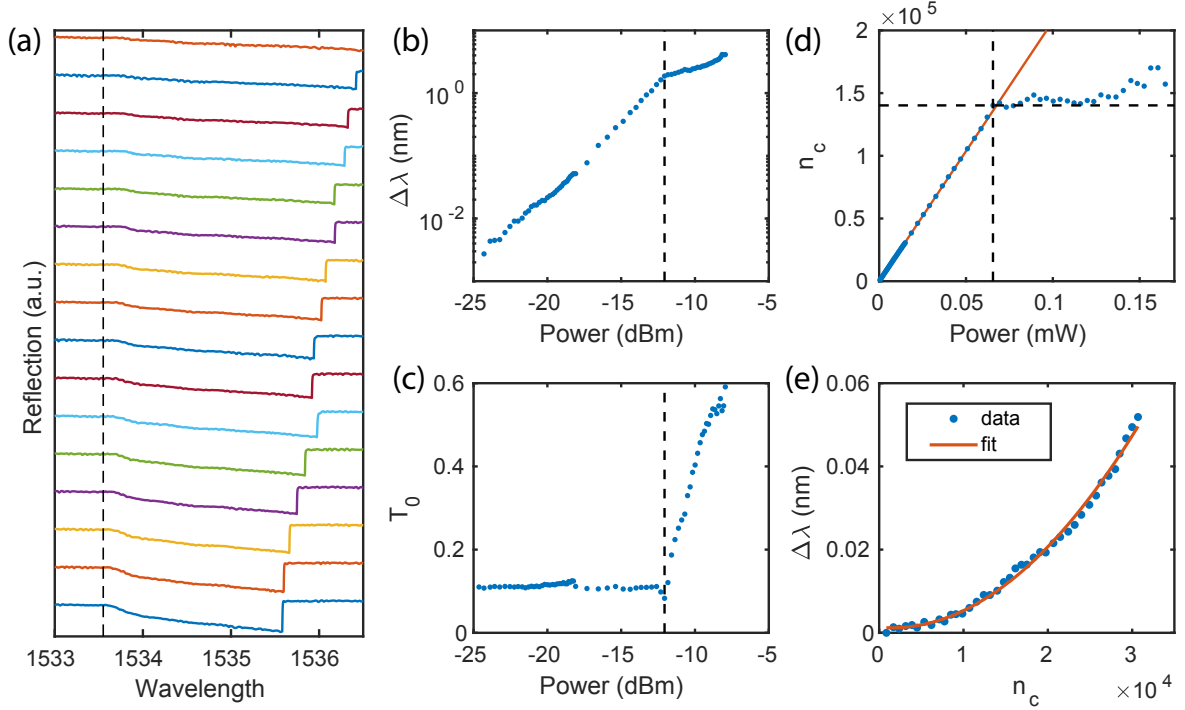


Fig. S5. Thermal-optical shift measurements. (a) Reflection signal of laser wavelength scan at increasing powers. Vertically displaced for viewing purposes. The vertical dashed line represents the cavity wavelength at low power. (b) Maximum optical cavity wavelength shift versus laser power, extracted from (a). (c) Minimum reflection T_0 at the resonance versus laser power, extracted from (a). (d) Maximal intracavity photon number versus laser power. (e) Wavelength shifts versus n_c before saturation (blue dots) and a quadratic fit (red line).

and intracavity photon number is obtained with $\Delta\lambda = \alpha_2 n_c^2$ where we call α_2 the quadratic thermal-induced cavity shift coefficient. $\alpha_2 \sim 6 \times 10^{-11} \text{ nm}/(\text{photon})^2$ is obtained from the fit. The cavity shift could also be expressed in terms of frequency shift $\Delta\omega_c = \alpha_2 n_c^2$ where $\alpha_2 \sim -7 \text{ Hz}/(\text{photon})^2$. We observed that the measured $\Delta\lambda$ is well characterized by the quadratic fit for $10^4 \lesssim n_c \lesssim 10^5$ and deviates from the fit at low and high power, showing that the actual thermal-induced cavity shift has a complicated dependency on n_c , including a small linear n_c term and also terms with higher order. The quadratic contribution already dominates the wavelength shift when the shift is noticeable with $\Delta\lambda \gtrsim \kappa$, making the linear term difficult to measure.

B. Measurement of the thermal relaxation rate

In this section we consider the response of the cavity to a laser pump with slow and weak amplitude modulation. We first define related parameters and variables in Table S1. When referring to the steady-state values at a constant power, quantities are denoted with a bar.

We start by assuming a linear thermal-optical shift of the optical cavity frequency with respect to temperature change

$$\Delta\omega_c = C_0 \Delta T. \quad (\text{S7})$$

Then dynamics of the temperature change is modeled by

$$\frac{d\Delta T}{dt} = -\Gamma \Delta T + f(n_c), \quad (\text{S8})$$

where $n_c = \kappa_e \dot{N}_{\text{in}} / (\Delta^2 + (\kappa/2)^2)$ is the instant intracavity photon number and $\dot{N}_{\text{in}} = P_{\text{in}} / (\hbar\omega_c)$ is the input photon flux of

the pump. An exponential temperature relaxation with rate Γ is assumed. We also assume that the heating effect only directly depends on intracavity photon number n_c via a general function f . The dynamical equation could be formulated in terms of the cavity shift $\Delta\omega_c$ as

$$\frac{d\Delta\omega_c}{dt} = -\Gamma \Delta\omega_c + C_0 f(n_c). \quad (\text{S9})$$

This equation describes the complicated dynamics of $\Delta\omega_c$ which also enters $f(n_c)$ implicitly via n_c . C_0 can be absorbed into the function f so that f has the dimension of $(\text{rad/s})^2$. We will omit C_0 from now on. Note that eq. S9 gives the steady-state cavity shift $\overline{\Delta\omega_c} = f(\bar{n}_c)/\Gamma$ from which we could solve $\Delta\omega_c$ and \bar{n}_c if f and Γ are known.

Based on eq. S9, we consider small time-dependent variations of laser power δP_{in} near the steady state solution. The laser wavelength is kept fixed. Note that n_c is a function of Δ and P_{in} so that

$$\frac{d\delta\Delta}{dt} = -\Gamma(\overline{\Delta\omega_c} + \delta\Delta) + f(\bar{n}_c) + f'(\bar{n}_c) \cdot \delta n_c \quad (\text{S10})$$

$$= -\Gamma\delta\Delta + f'(\bar{n}_c) \cdot \left(\frac{\bar{n}_c \delta P_{\text{in}}}{P_{\text{in}}} - \frac{2\bar{n}_c \bar{\Delta} \delta\Delta}{\bar{\Delta}^2 + (\kappa/2)^2} \right) \quad (\text{S11})$$

$$= -(\Gamma + \Gamma_2)\delta\Delta + f'(\bar{n}_c) \bar{n}_c \cdot \frac{\delta P_{\text{in}}}{P_{\text{in}}}, \quad (\text{S12})$$

where

$$\Gamma_2 = \frac{2\bar{\Delta}}{\bar{\Delta}^2 + (\kappa/2)^2} \cdot f'(\bar{n}_c) \bar{n}_c = g(\bar{\Delta}) \cdot h(\bar{n}_c). \quad (\text{S13})$$

Table S1. Definition of parameters related to thermal relaxation rate measurements.

Parameter	Description	Useful relation
P_{in}	input laser power	
ΔT	temperature change	
$\Delta\omega_c$	thermal-induced cavity shift	$\Delta\omega_c = \alpha_1 n_c + \alpha_2 n_c^2$
Δ	real-time cavity-laser detuning	$\Delta = \omega_c - \omega_l + \Delta\omega_c$
\dot{N}_{in}	input photon flux	$P_{\text{in}}/(\hbar\omega_l)$
n_c	intracavity photon number	$n_c = \kappa_e \dot{N}_{\text{in}}/(\Delta^2 + (\kappa/2)^2)$
δP_{in}	small laser power variation	
δn_c	small n_c variation due to δP_{in}	
$\delta\omega_c$	extra cavity shift variation due to δn_c	
$\delta\Delta$	small detuning variation	$\delta\Delta = \delta\omega_c$ for fixed laser wavelength
Γ	temperature relaxation rate	
Γ_2	measurement induced extra relaxation rate	
Γ_{tot}	total measured relaxation rate	$\Gamma_{\text{tot}} = \Gamma + \Gamma_2$

The extra relaxation rate Γ_2 reflects the fact that the laser amplitude-modulation measurement method enters the complicated dynamics of the system itself, leading to an effective relaxation rate in addition to the actual relaxation rate Γ . We define functions g and h to represent the dependency of Γ_2 on $\bar{\Delta}$ and \bar{n}_c . We point out that $\bar{\Delta}$ and \bar{n}_c can be independently controlled by preparing the steady state with different laser frequencies ω_l and powers P_{in} .

When the input laser power has a small variation $\delta P_{\text{in}} = \alpha \cos(\omega t)$, by assuming $\delta\Delta = \beta \cos(\omega t + \phi)$ and plugging into eq. S12, we get the amplitude response of $\delta\Delta$ to δP_{in} to be

$$\left| \frac{\beta}{\alpha} \right| \propto \frac{1}{\sqrt{\omega^2 + (\Gamma + \Gamma_2)^2}}. \quad (\text{S14})$$

As a result, the total ‘‘relaxation rate’’ $\Gamma_{\text{tot}} = \Gamma + \Gamma_2$ can be measured from the low-frequency amplitude response of $\delta\Delta$. With the measurement of Γ_{tot} and independent control over $\bar{\Delta}$ and \bar{n}_c , we are allowed to probe the structure of Γ_2 and thus the unknown function f .

Proceeding to the determination of f , we assume a polynomial form $f(n) = a_1 n + a_2 n^2 + O(n^3)$, where higher order terms are assumed to be small based on the steady-state cavity shift measurements. With this assumption, $h(n) = n f'(n) = a_1 n + 2a_2 n^2$, and

$$\Gamma_{\text{tot}} = (1, g(\bar{\Delta})\bar{n}_c, 2g(\bar{\Delta})\bar{n}_c^2) \cdot (\Gamma, a_1, a_2)^T = \mathbf{M} \cdot \mathbf{b}. \quad (\text{S15})$$

By carrying out multiple measurements of Γ_{tot} with different \mathbf{M} , the thermal relaxation rate Γ and coefficients a_1 and a_2 can be determined by solving a linear regression problem. Once Γ, a_1 and a_2 are obtained, the steady-state cavity shift is $\Delta\omega_c = a_1 \bar{n}_c + a_2 \bar{n}_c^2 = a_1 \bar{n}_c / \Gamma + a_2 \bar{n}_c^2 / \Gamma$.

We now show that the response of $\delta\Delta$ can be directly measured by the same coherent spectroscopy setup at low modulation frequencies. When there is no slow thermal-induced cavity wavelength shift, the optical response is given by

$$r(\omega \ll \Delta) \approx 1 - \frac{\kappa_e}{i(\Delta - \omega) + \kappa/2}. \quad (\text{S16})$$

When the slow cavity wavelength shift is considered, Δ is replaced by $\bar{\Delta} + \delta\Delta(\omega)$, where $\delta\Delta(\omega)$ is the frequency-domain response of the slow thermal-induced wavelength shift. For small and low-frequency intensity modulation, we assume $\omega \ll \delta\Delta \ll \Delta$, and the response can be simplified as

$$\begin{aligned} r(\omega \ll \Delta) &\approx 1 - \frac{\kappa_e}{i(\bar{\Delta} + \delta\Delta(\omega)) + \kappa/2} \quad (\text{S17}) \\ &\approx 1 - \frac{\kappa_e}{i\bar{\Delta} + \kappa/2} + \frac{\kappa_e}{i\bar{\Delta} + \kappa/2} \cdot \frac{i\delta\Delta(\omega)}{i\bar{\Delta} + \kappa/2}. \quad (\text{S18}) \end{aligned}$$

The resulting intensity response is

$$|r(\omega \ll \Delta)|^2 = A + B \cdot \delta\Delta(\omega) + O\left(\left(\frac{\delta\Delta}{\Delta}\right)^2\right), \quad (\text{S19})$$

where A and B are two real-valued functions of Δ, κ and κ_e . The exact forms of A and B are involving but not important since they are approximately independent of frequency for $\omega \ll \Delta$. As a result, for low frequency intensity modulation, the only frequency-dependent intensity response is from the variation of thermal-induced cavity shift $\delta\Delta = \delta\omega_c$.

We measured the intensity response $|r(\omega \ll \Delta)|^2$ for frequency range 100 kHz \sim 5 MHz. The amplitude of the response is fitted to a Lorentzian centered at frequency $f = 0$. The linewidth of this Lorentzian corresponds to the total relaxation rate Γ_{tot} . A typical low frequency response is shown in fig. S6(a) with the Lorentzian fit (red). In this way we extracted Γ_{tot} under different laser powers and wavelengths. The steady-state cavity-laser detuning $\bar{\Delta}$ is measured at the same time by an optical sideband sweep across the cavity. With measured $\Gamma_{\text{tot}}, \bar{\Delta}$ and \bar{n}_c , the linear regression problem eq. S15 is solved. We obtain the true thermal relaxation rate $\Gamma = 150$ kHz, linear thermal-induced cavity shift coefficient $\alpha_1 = a_1/\Gamma \approx -7.1 \times 10^4$ Hz/photon and quadratic thermal-induced cavity shift coefficient $\alpha_2 = a_2/\Gamma \approx -1.5$ Hz/(photon)².

The thermal relaxation rate Γ quantitatively agrees with the thermal-optical response time scale of ~ 10 μ s reported in

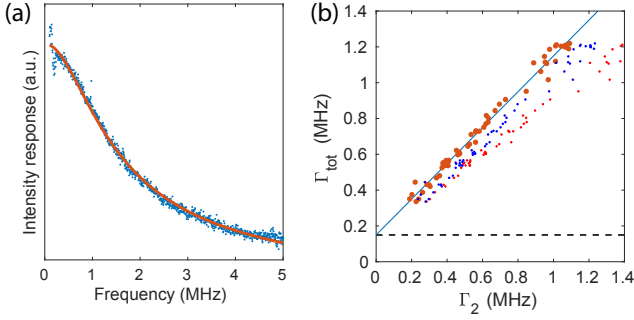


Fig. S6. Measurement of thermal relaxation rate. (a) Example of low frequency intensity modulation response of the OMC system. Blue: data. Red: Lorentzian fit. (b) Measured total relaxation rate versus measurement induced extra relaxation rate (orange). The black dashed line shows the actual thermal relaxation rate of the OMC. The blue line is a guide for the eye and has a slope of 1.

Ref. [S5] and is slightly faster due to smaller device volume. We note that for $n_c \gtrsim 5 \times 10^4$, the thermal-optical shift starts to be dominated by the quadratic contribution, which agrees with the steady-state wavelength shift measurement in the last section. We note that the a_2 obtained here is smaller than the value from steady-state wavelength shift measurement by a factor ~ 4 .

We further calculated Γ_2 with a_1 and a_2 from the linear regression and n_c from the measurements. We show in fig. S6(b) the measured Γ_{tot} versus calculated Γ_2 (orange dots). The horizontal black dashed line corresponds to the constant Γ . A blue line starting at $(0, \Gamma)$ with slope equals to one is plotted for guide of the eye. It's clear that good agreement is obtained between the linear regression results and the equation $\Gamma_{\text{tot}} = \Gamma + \Gamma_2$, under a large variation of both laser powers and cavity-laser detunings. To show the reliability of the linear regression results, we manually increase the obtained value of a_1 (a_2) by 50% and plot the modified Γ_2 in fig. S6(b) as small blue (red) dots for comparison. Deviation from $\Gamma_{\text{tot}} = \Gamma + \Gamma_2$ can be clearly observed.

3. MEASUREMENT OF OPTICAL LINEWIDTH WITH DIFFERENT INTRACAVITY PHOTON NUMBERS

In sec. 2A we observed the minimal transmission T_0 increased for high laser powers. We further deduced the minimal cavity-laser detunings before the optical mode jumped back to the blue side of the laser based on the minimal transmission measurements. However, a change in the cavity intrinsic linewidth κ_i could also change the transmission dip, where $T_0|_{\Delta=0} = |(\kappa/2 - \kappa_e)/(\kappa/2)|^2 = |(\kappa_i - \kappa_e)/(\kappa_i + \kappa_e)|^2$. To track any considerable change in the cavity intrinsic linewidth, we fit the probe response from the coherent spectroscopy with different pump laser powers and different cavity-laser detunings. This two-tone spectroscopy effectively gives us the linear response of the cavity at different pump powers and helps us determine Δ , κ_e , and κ_i , as a function of laser power and detuning.

Fig. S7(a) shows one typical phase response of the probe with a high pump laser power $P_{\text{in}} = 0.21$ mW and a small cavity-laser detuning $\Delta \sim -\kappa$. By fitting the phase response (red), we extract the total optical linewidth κ . Measurements of κ versus intracavity photon numbers n_c with various pump powers and detunings are plotted in fig. S7(b). Different colors correspond

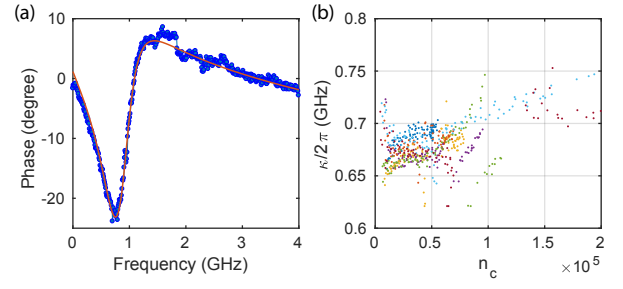


Fig. S7. Measurement of optical linewidth κ with different intracavity photon numbers n_c . (a) A typical phase response of the probe with a high pump power $P_{\text{in}} \sim 0.2$ mW and a near-cavity detuning $\Delta \sim \kappa$. The red line shows the fit result. (b) Extracted total optical linewidth κ versus different intracavity photon numbers n_c under different pump powers and detunings. Different colors correspond to different pump laser powers.

to different pump laser powers ranging from 96 μ W to 0.21 mW. We obtained $\kappa/2\pi \approx 0.7$ GHz with relative standard deviation $\sim 9\%$ for all measurements with different pump powers. A linear increase in total linewidth for increasing n_c can be observed and shows different slopes for different pump powers. We note that in general the optical linewidth varies by less than 15% for n_c varying more than two orders of magnitude.

4. COUPLING AND CONVERSION BETWEEN MICROWAVE, MECHANICS AND OPTICS

A. Input-output formalism of a optomechanical crystal coupling to a microwave resonator or a microwave channel

Consider a system with an OMC coupling to a microwave resonator c with coupling strength g_μ . We start by writing down the frequency-domain Heisenberg-Langevin equations of motion in a rotating frame at the laser frequency for $\Delta \sim \omega_m$:

$$-i\omega a(\omega) = -(i\Delta + \frac{\kappa}{2})a - iGb - \sqrt{\kappa_e}a_{\text{in}} \quad (\text{S20})$$

$$-i\omega b(\omega) = -(i\omega_m + \frac{\gamma}{2})b - iGa - ig_\mu c - \sqrt{\gamma_e}b_{\text{in}} \quad (\text{S21})$$

$$-i\omega c(\omega) = -(i\omega_\mu + \frac{\kappa_\mu}{2})c - ig_\mu b - \sqrt{\kappa_{\mu,e}}c_{\text{in}} \quad (\text{S22})$$

We assume that every mode is coupled to a single external channel respectively. The counter-rotating terms have been omitted for simplicity. We introduce short-hands

$$A_a = i(\Delta - \omega) + \kappa/2 \quad (\text{S23})$$

$$A_b = i(\omega_m - \omega) + \gamma/2 \quad (\text{S24})$$

$$A_c = i(\omega_\mu - \omega) + \kappa_\mu/2 \quad (\text{S25})$$

$$\eta_{ab} = -iG/A_a \quad (\text{S26})$$

$$\eta_{ba} = -iG/A_b \quad (\text{S27})$$

$$\eta_{bc} = -ig/A_b \quad (\text{S28})$$

$$\eta_{cb} = -ig/A_c \quad (\text{S29})$$

$$\eta_{ijk} = \eta_{ij}\eta_{jk} \quad (\text{S30})$$

where i, j, k run through a, b, c . With them the solution can be expressed as

$$\begin{bmatrix} a \\ b \\ c \end{bmatrix} = \frac{1}{1 - \eta_{aba} - \eta_{bcb}} \begin{bmatrix} 1 - \eta_{bcb} & \eta_{ab} & \eta_{abc} \\ \eta_{ba} & 1 & \eta_{bc} \\ \eta_{cba} & \eta_{cb} & 1 - \eta_{aba} \end{bmatrix} \begin{bmatrix} -\frac{\sqrt{\kappa_e} a_{in}}{A_a} \\ -\frac{\sqrt{\gamma_e} b_{in}}{A_b} \\ -\frac{\sqrt{\kappa_{\mu,e}} c_{in}}{A_c} \end{bmatrix} \quad (\text{S31})$$

From eq. S31, we can directly read the electro-optic conversion S parameters when only input c_{in} or a_{in} presents:

$$S_{ac} \equiv \frac{a_{out}}{c_{in}} = \frac{\sqrt{\kappa_e} a}{c_{in}} \quad (\text{S32})$$

$$= \sqrt{\kappa_e} \frac{\eta_{abc}}{1 - \eta_{aba} - \eta_{bcb}} \frac{-\sqrt{\kappa_{\mu,e}}}{A_c} \quad (\text{S33})$$

$$= \sqrt{\kappa_e} \frac{1}{A_a} \frac{G g_{\mu}}{A_b + G^2/A_a + g_{\mu}^2/A_c} \frac{1}{A_c} \sqrt{\kappa_{\mu,e}} \quad (\text{S34})$$

$$= S_{ca} \equiv \frac{c_{out}}{a_{in}} \quad (\text{S35})$$

At perfectly matched frequencies $\omega = \Delta = \omega_m = \omega_{\mu}$, we have the conversion efficiency

$$\eta \equiv |S_{ac}|^2 = |S_{ca}|^2 \quad (\text{S36})$$

$$= \kappa_e \frac{4}{\kappa^2} \frac{4G^2 g_{\mu}^2 / \gamma^2}{(1 + 4G^2 / \kappa \gamma + 4g_{\mu}^2 / \kappa_{\mu} \gamma)^2} \frac{4}{\kappa_{\mu}^2} \kappa_{\mu,e} \quad (\text{S37})$$

$$= \eta_{ext,a} \eta_{ext,c} \frac{4C_{ab} C_{bc}}{(1 + C_{ab} + C_{bc})^2} \quad (\text{S38})$$

where $\eta_{ext,a} = \kappa_e / \kappa$ and $\eta_{ext,c} = \kappa_{\mu,e} / \kappa_{\mu}$ are defined as the external efficiencies. C_{ab} (C_{bc}) is the cooperativity between the mechanical mode and the optical (microwave) mode. The maximal conversion efficiency $\eta = \eta_{ext,a} \eta_{ext,c}$ is achieved for $C_{ab} = C_{bc} \gg 1$.

We proceed to consider the simplified case where the mechanical mode is directly coupled to a microwave channel. The external decay rate γ_e now represents the coupling between the microwave channel and the mechanical mode. The equations of motion read

$$-i\omega a(\omega) = -(i\Delta + \frac{\kappa}{2})a - iGb - \sqrt{\kappa_e} a_{in} \quad (\text{S39})$$

$$-i\omega b(\omega) = -(i\omega_m + \frac{\gamma}{2})b - iGa - \sqrt{\gamma_e} c_{in} \quad (\text{S40})$$

and the simplified version of eq. S31 is

$$\begin{bmatrix} a \\ b \end{bmatrix} = \frac{1}{1 - \eta_{aba}} \begin{bmatrix} 1 & \eta_{ab} \\ \eta_{ba} & 1 \end{bmatrix} \begin{bmatrix} -\frac{\sqrt{\kappa_e} a_{in}}{A_a} \\ -\frac{\sqrt{\gamma_e} c_{in}}{A_b} \end{bmatrix}. \quad (\text{S41})$$

Similarly, the electro-optic S parameter is

$$S_{ac} = \sqrt{\kappa_e} \frac{\eta_{ab}}{1 - \eta_{aba}} \frac{-\sqrt{\gamma_e}}{A_b} \quad (\text{S42})$$

$$= \sqrt{\kappa_e} \frac{1}{A_a} \frac{iG}{A_b + G^2/A_a} \sqrt{\gamma_e} \quad (\text{S43})$$

The resulting conversion efficiency at perfectly-matched frequency $\omega = \Delta = \omega_m$ is

$$\eta = \kappa_e \frac{4}{\kappa^2} \frac{4G^2 / \gamma^2}{(1 + 4G^2 / \kappa \gamma)^2} \gamma_e \quad (\text{S44})$$

$$= \eta_{ext,a} \eta_{ext,b} \frac{4C_{ab}}{(1 + C_{ab})^2} \quad (\text{S45})$$

where $\eta_{ext,b} = \gamma_e / \gamma$. The maximum of conversion efficiency occurs at the matching condition $C_{ab} = 1$, where similarly $\eta = \eta_{ext,a} \eta_{ext,b}$.

B. Measurement of coupling between the mechanical resonator and a microwave channel

Our OMC can be coupled to a microwave channel via the piezoelectric interaction. We evaporated electrode on both ends of the nanobeam and connected them to a transmission line with impedance $Z_0 = 50 \Omega$. The electric field generated by the electrode is parallel to the nanobeam. The same configuration can also be adopted for coupling the mechanical resonator to microwave circuits.

From the last section, with $\Delta = \omega_m$, the coherent mechanical field amplitude is

$$\beta = \frac{-\sqrt{\gamma_e} c_{in}}{i(\omega_m - \omega_{\mu}) + \gamma_{tot}/2}, \quad (\text{S46})$$

where c_{in} is the input microwave amplitude with a unit of $1/\sqrt{\text{Hz}}$, $\gamma_{tot} = \gamma_i + \gamma_e + \gamma_{OM}$ is the total mechanical linewidth and $\omega_{\mu} \approx \omega_m$ is the microwave signal frequency. The resulting coherent phonon number in the mechanical mode is

$$n_{coh} = |\beta|^2 = \frac{\gamma_e \dot{N}_{\mu}}{(\omega_{\mu} - \omega_m)^2 + (\gamma_{tot}/2)^2}, \quad (\text{S47})$$

where $\dot{N}_{\mu} = |c_{in}|^2 = \eta_{loss} P_{\mu} / (\hbar \omega_{\mu})$ is the input microwave photon flux, P_{μ} is the output power of the VNA and $\eta_{loss} \approx 58\%$ accounts for external RF cable loss. We tune $\omega_{\mu} = \omega_m$ and measure the transduced optical sideband power spectral density of both the coherent phonons and thermal phonons using the RSA. The microwave-to-mechanics coupling rate is given by

$$\gamma_e = \frac{n_{coh} \gamma_{tot}^2}{4 \dot{N}_{\mu}}. \quad (\text{S48})$$

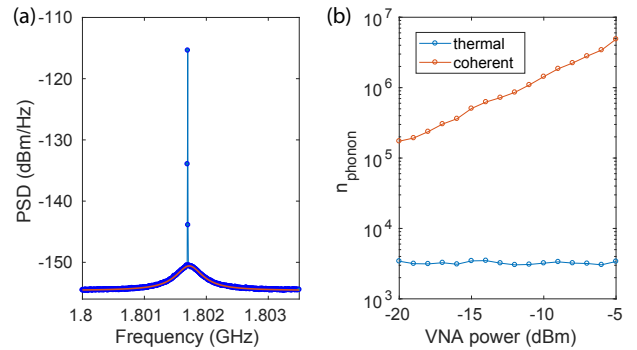


Fig. S8. Microwave to mechanics conversion. (a) Measured power spectral density of thermal mechanical motion and coherent mechanical motion from the piezoelectric drive. Blue: data, red: Lorentzian fit of the thermal motion peak. (b) Extracted phonon numbers from the power spectral density for different VNA drive power.

Fig. S8(a) shows a measured optical sideband power spectral density (PSD). The thermal mechanical motion give rise to the broad Lorentzian peak and the coherent RF drive corresponds to the sharp peak. We integrate the sideband RF power under

both the thermal peak P_{therm} and the coherent peak P_{coh} independently. The thermal occupancy of the mechanical mode is calculated by $n_{\text{therm}} = k_B T / \hbar \omega_m \approx 3400$ with $T = 295$ K. The optical and electrical gain of the whole readout chain is then determined by $G = \langle P_{\text{therm}} \rangle / n_{\text{therm}}$ for a certain optical pump power. We drive the OMC with different RF powers and extract the thermal and coherent phonon numbers from the PSD in fig. S8(b). The coherent phonon numbers rise linearly with the increasing RF powers while the thermal phonon occupancies stay near-constant. We obtained $\gamma_e / 2\pi = 8.8 \pm 0.56$ mHz.

C. Estimating coupling between the LN OMC and a microwave resonator or a superconducting qubit

In this section we estimate the coupling of the mechanical mode to a microwave resonator or a superconducting qubit based on our measurement of γ_e in the last section.

The mechanical resonator is commonly modeled as a parallel LC resonator [S6]. To take into account the non-zero energy decay rate γ , a resistor is added in parallel such that $\gamma = 1/(RC)$. The mechanical resonator can be coupled to an external 50 Ω transmission line through coupling capacitance C_g , as shown in fig. S9(a). The external coupling introduces a frequency shift and an additional decay rate from an effective conductance $1/Z_e = \omega_m^2 C_g^2 Z_0$ [S7]. From this equivalence, we obtain a relationship between the coupling capacitance C_g and the coupling induced decay rate $\gamma_e = \omega_m^2 C_g^2 Z_0 / C$.

We show in fig. S9(e) a mechanical resonator coupling to a microwave resonator or a superconducting qubit. The coupling rate is given by [S8]

$$g \simeq \sqrt{\omega_m \omega_2} \cdot \frac{C_g}{2\sqrt{(C + C_g)(C_2 + C_g)}} \quad (\text{S49})$$

$$\approx \sqrt{\omega_m \omega_2} \cdot \frac{C_g}{2\sqrt{CC_2}}, \quad (\text{S50})$$

where we've made the assumption that $C_g \ll C_1, C_2$. To simplify the result, we assume that the two modes are perfectly matched with $\omega_2 = \omega_m$, and the microwave resonator has a characteristic impedance $Z_c = \sqrt{L_2/C_2}$. As a result,

$$g^2 = \frac{\omega_m^2 C_g^2}{C} \cdot \frac{1}{4C_2} = \frac{\gamma_e}{Z_0} \cdot \frac{\omega_m Z_c}{4}, \quad (\text{S51})$$

where we made the substitution $1/C_2 = \omega_2 Z_c$.

In conclusion, the coupling rate between a mechanical resonator and a microwave channel γ_e and the coupling rate between a mechanical resonator and a microwave resonator g are related by $g = \sqrt{\gamma_e \omega_m} \sqrt{Z_c / Z_0} / 2$.

5. EXTRACTING PUMP DETUNINGS FROM ON-CHIP ELECTRO-OPTIC MODULATION

We start with the electro-optic interaction Hamiltonian. The perturbation on the optical mode frequency from a voltage V across the electrodes are modeled by

$$H_{\text{EO}} = \hbar \frac{d\omega}{dV} V \hat{a}^\dagger \hat{a} \quad (\text{S52})$$

$$= -i\hbar \sqrt{\kappa_{e,\mu}} \hat{a}^\dagger \hat{a} (c_{\text{in}} - c_{\text{in}}^\dagger). \quad (\text{S53})$$

Where we rewrite the voltage in terms of input microwave amplitude c_{in} and choose a specific phase of c_{in} for later convenience. After linearization and rotating wave approximation:

$$H_{\text{EO}} = -i\hbar \sqrt{\kappa_{e,\mu}} (\alpha_0 \hat{a}^\dagger c_{\text{in}} - \alpha_0^* \hat{a} c_{\text{in}}^\dagger). \quad (\text{S54})$$

where $\alpha_0 = -\sqrt{\kappa_e} \alpha_{\text{in}} / (i\Delta + \kappa/2)$ is the optical intracavity pump amplitude and α_{in} is the pump input photon amplitude. Equation of motion for the optical sideband amplitude is

$$-i\omega a(\omega) = -(i\Delta + \frac{\kappa}{2})a - \sqrt{\kappa_{e,\mu}} \alpha_0 c_{\text{in}} \quad (\text{S55})$$

from which we could solve the sideband amplitude and calculate the output optical field as

$$\begin{aligned} \alpha_{\text{out}} &= \left[1 - \frac{\kappa_e}{i\Delta + \frac{\kappa}{2}} \left(1 - \frac{\sqrt{\kappa_{e,\mu}}}{i(\Delta - \omega_\mu) + \frac{\kappa}{2}} c_{\text{in}} e^{-i\omega_\mu t} \right) \right] \alpha_{\text{in}} \\ &= \left(r(\Delta) + s_{\text{EO}}(\omega_\mu, \Delta) c_{\text{in}} e^{-i\omega_\mu t} \right) \alpha_{\text{in}}, \end{aligned} \quad (\text{S56})$$

where

$$r(\Delta) = 1 - \frac{\kappa_e}{i\Delta + \kappa/2}, \quad (\text{S57})$$

$$s_{\text{EO}}(\omega, \Delta) = \frac{\kappa_e}{i\Delta + \kappa/2} \frac{\sqrt{\kappa_{e,\mu}}}{i(\Delta - \omega) + \frac{\kappa}{2}}. \quad (\text{S58})$$

The electronic signal from the high-speed photo-detector is

$$\begin{aligned} V_{\text{HS}} &= G |\alpha_{\text{out}}|^2 = G |\alpha_{\text{in}}|^2 \left(|r(\Delta)|^2 + \right. \\ &\quad \left. r^*(\Delta) s_{\text{EO}}(\omega_\mu, \Delta) c_{\text{in}} e^{-i\omega_\mu t} + h.c. + O(c_{\text{in}}^2) \right) \end{aligned} \quad (\text{S59})$$

where G denotes the total detection gain. As a result, the VNA directly measures $S_{21}(\omega, \Delta) \propto G |\alpha_{\text{in}}|^2 r^*(\Delta) s_{\text{EO}}(\omega, \Delta) S_{\text{ext}}(\omega)$ where we further include the external response of the cables and wirebonds in $S_{\text{ext}}(\omega)$.

For the coherent spectroscopy, the external response and the detection gain can be removed by dividing the response with a background taken with far-detuned pump laser [S3, S9]. The electro-optic (EO) sideband is generated by the EOM and doesn't depend on the cavity-laser detuning. However, for the on-chip EO modulation, the intracavity photon numbers are much smaller for far-detuned pump laser, resulting in a much weaker EO sideband and a very low SNR. To eliminate the detection gain G and the external response, we take the ratio between two S_{21} measurements with different near-cavity detunings Δ_1 and Δ_2 where $|\Delta_1 - \Delta_2| \gtrsim \kappa$. The gain and external response is identical and cancels, leaving only the ratio of the on-chip EO response. We denote the ratio of the S_{21} as

$$S_{\Delta_2/\Delta_1}(\omega) = \frac{r^*(\Delta_2) s_{\text{EO}}(\omega, \Delta_2)}{r^*(\Delta_1) s_{\text{EO}}(\omega, \Delta_1)}. \quad (\text{S60})$$

By fitting the measured S_{21} ratio with different detunings and identical pump laser power, we extract both detunings Δ_1 and Δ_2 .

In fig. S10 we show a typical measured S_{Δ_2/Δ_1} (blue) and the fitting results using eq. S60 (red). The external responses are perfectly removed, allowing us to extract the detunings of the pump laser. We point out that with the piezoelectric drive off, the pump detunings could also be extracted using the external EOM sideband sweep as used in the coherent spectroscopy.

REFERENCES

- [S1] J. Chan, A. H. Safavi-Naeini, J. T. Hill, S. Meenehan, and O. Painter, "Optimized optomechanical crystal cavity with acoustic radiation shield," *Appl. Phys. Lett.* **101**, 081115 (2012).

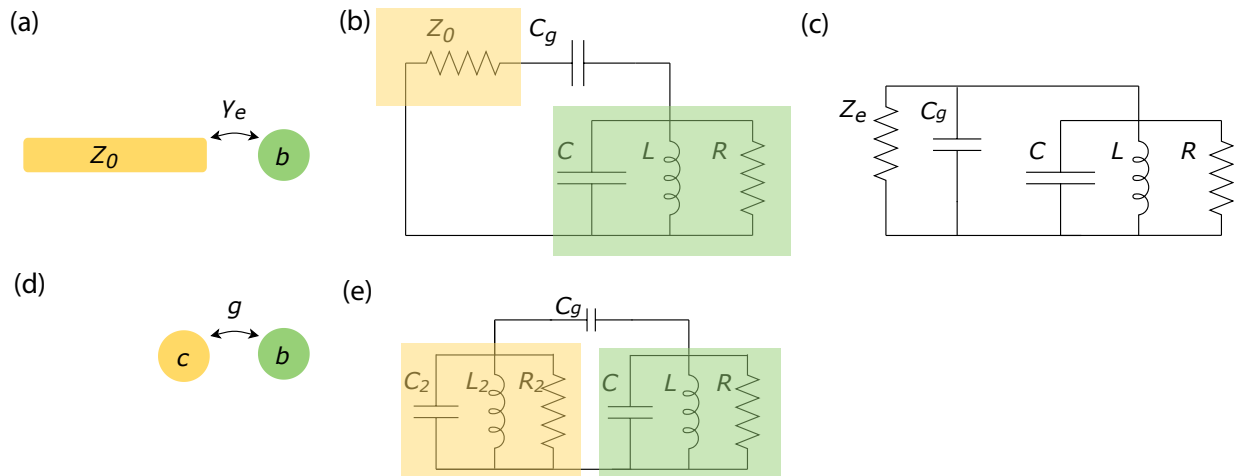


Fig. S9. Coupling between mechanics and microwave. (a) A mechanical resonator (green) coupled to a microwave channel (yellow). (b) Circuit model of (a). (c) Equivalent circuit of (b). (d) A mechanical resonator (green) coupled to a microwave resonator (yellow). (e) Circuit model of (d).

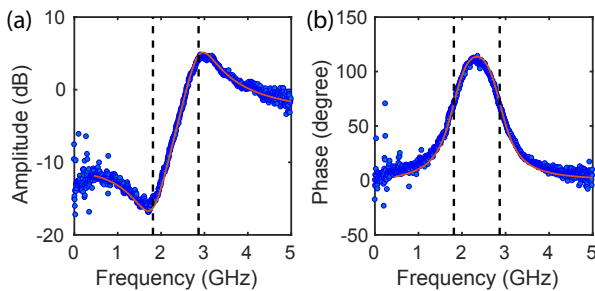


Fig. S10. On-chip electro-optic response and fit. (a) Amplitude and (b) phase of the electro-optic response. Red curves show the fitting results. The detunings extracted from the fit are shown as black vertical dashed lines for comparison.

ultrastrong coupling in transmon circuit qed using a high-impedance resonator," *Phys. Rev. B* **95**, 224515 (2017).

[S9] J. Chan, "Laser cooling of an optomechanical crystal resonator to its quantum ground state of motion," Ph.D. thesis, California Institute of Technology (2012).

[S10] R. Weis and T. Gaylord, "Lithium niobate: Summary of physical properties and crystal structure," *Appl. Phys. A* **37**, 191–203 (1985).

[S11] W. R. Inc., "Mathematica," Available from <http://www.wolfram.com>.

[S2] A. Andrushchak, B. Mytsyk, H. Laba, O. Yurkevych, I. Soltskii, A. Kityk, and B. Sahraoui, "Complete sets of elastic constants and photoelastic coefficients of pure and mgo-doped lithium niobate crystals at room temperature," *J. Appl. Phys.* **106**, 073510 (2009).

[S3] R. N. Patel, Z. Wang, W. Jiang, C. J. Sarabalis, J. T. Hill, and A. H. Safavi-Naeini, "Single-mode phononic wire," *Phys. Rev. Lett.* **121**, 040501 (2018).

[S4] T. Carmon, L. Yang, and K. J. Vahala, "Dynamical thermal behavior and thermal self-stability of microcavities," *Opt. Express* **12**, 4742–4750 (2004).

[S5] X. Sun, H. Liang, R. Luo, W. C. Jiang, X.-C. Zhang, and Q. Lin, "Nonlinear optical oscillation dynamics in high-q lithium niobate microresonators," *Opt. Express* **25**, 13504–13516 (2017).

[S6] P. Arrangoiz-Arriola, E. A. Wollack, M. Pechal, J. D. Witmer, J. T. Hill, and A. H. Safavi-Naeini, "Coupling a superconducting quantum circuit to a phononic crystal defect cavity," *Phys. Rev. X* **8**, 031007 (2018).

[S7] D. I. Schuster, *Circuit quantum electrodynamics* (Yale University, 2007).

[S8] S. J. Bosman, M. F. Gely, V. Singh, D. Bothner, A. Castellanos-Gomez, and G. A. Steele, "Approaching

6. ROTATED PHOTOELASTIC TENSOR COMPONENTS

The original photoelastic tensor components are given by [S10]

$$p = \begin{bmatrix} p_{11} & p_{12} & p_{13} & p_{14} & 0 & 0 \\ p_{12} & p_{11} & p_{13} & -p_{14} & 0 & 0 \\ p_{31} & p_{31} & p_{33} & 0 & 0 & 0 \\ p_{41} & -p_{41} & 0 & p_{44} & 0 & 0 \\ 0 & 0 & 0 & 0 & p_{44} & p_{41} \\ 0 & 0 & 0 & 0 & p_{14} & (p_{11} - p_{12})/2 \end{bmatrix}. \quad (\text{S61})$$

Using the rotation matrix and MATHEMATICA [S11], we obtain the rotated photoelastic components in the contracted index notation for X-cut LN as

$$p'_{\text{LNX}} = \begin{bmatrix} p'_{11} & p'_{12} & p'_{13} & 0 & 0 & p'_{16} \\ p'_{21} & p'_{22} & p'_{23} & 0 & 0 & p'_{26} \\ p'_{31} & p'_{32} & p'_{33} & 0 & 0 & p'_{36} \\ 0 & 0 & 0 & p'_{44} & p'_{45} & 0 \\ 0 & 0 & 0 & p'_{54} & p'_{55} & 0 \\ p'_{61} & p'_{62} & p'_{63} & 0 & 0 & p'_{66} \end{bmatrix}, \quad (\text{S62})$$

with

$$p'_{11} = p_{11} \sin^4(\phi) + p_{44} \sin^2(2\phi) + p_{33} \cos^4(\phi) + p_{13} \sin^2(\phi) \cos^2(\phi) + p_{31} \sin^2(\phi) \cos^2(\phi) - 2p_{14} \sin^3(\phi) \cos(\phi) - 2p_{41} \sin^3(\phi) \cos(\phi), \quad (\text{S63})$$

$$p'_{12} = p_{13} \sin^4(\phi) - p_{44} \sin^2(2\phi) + p_{31} \cos^4(\phi) - 2p_{41} \sin(\phi) \cos^3(\phi) + p_{11} \sin^2(\phi) \cos^2(\phi) + p_{33} \sin^2(\phi) \cos^2(\phi) + 2p_{14} \sin^3(\phi) \cos(\phi) \quad (\text{S64})$$

$$p'_{13} = p_{12} \sin^2(\phi) + p_{41} \sin(2\phi) + p_{31} \cos^2(\phi) \quad (\text{S65})$$

$$p'_{16} = \sin(\phi) \left(-p_{31} \cos^3(\phi) + p_{33} \cos^3(\phi) - 2p_{44} \cos(2\phi) \cos(\phi) + 2p_{41} \sin(\phi) \cos^2(\phi) - p_{11} \sin^2(\phi) \cos(\phi) + p_{13} \sin^2(\phi) \cos(\phi) + p_{14} \sin(\phi) \cos(2\phi) \right) \quad (\text{S66})$$

$$p'_{21} = p_{31} \sin^4(\phi) - p_{44} \sin^2(2\phi) + p_{13} \cos^4(\phi) - 2p_{14} \sin(\phi) \cos^3(\phi) + p_{11} \sin^2(\phi) \cos^2(\phi) + p_{33} \sin^2(\phi) \cos^2(\phi) + 2p_{41} \sin^3(\phi) \cos(\phi) \quad (\text{S67})$$

$$p'_{22} = p_{33} \sin^4(\phi) + p_{44} \sin^2(2\phi) + p_{11} \cos^4(\phi) + 2p_{14} \sin(\phi) \cos^3(\phi) + 2p_{41} \sin(\phi) \cos^3(\phi) + p_{13} \sin^2(\phi) \cos^2(\phi) + p_{31} \sin^2(\phi) \cos^2(\phi) \quad (\text{S68})$$

$$p'_{23} = p_{12} \cos^2(\phi) + \sin(\phi) (p_{31} \sin(\phi) - 2p_{41} \cos(\phi)) \quad (\text{S69})$$

$$p'_{26} = \cos(\phi) \left(-p_{31} \sin^3(\phi) + p_{33} \sin^3(\phi) + p_{14} \cos(\phi) \cos(2\phi) - p_{11} \sin(\phi) \cos^2(\phi) + p_{13} \sin(\phi) \cos^2(\phi) - 2p_{41} \sin^2(\phi) \cos(\phi) + 2p_{44} \sin(\phi) \cos(2\phi) \right) \quad (\text{S70})$$

$$p'_{31} = p_{12} \sin^2(\phi) + p_{14} \sin(2\phi) + p_{13} \cos^2(\phi) \quad (\text{S71})$$

$$p'_{32} = p_{12} \cos^2(\phi) + \sin(\phi) (p_{13} \sin(\phi) - 2p_{14} \cos(\phi)) \quad (\text{S72})$$

$$p'_{33} = p_{11} \quad (\text{S73})$$

$$p'_{36} = \frac{1}{2} (p_{12}(-\sin(2\phi)) + p_{13} \sin(2\phi) - 2p_{14} \cos(2\phi)) \quad (\text{S74})$$

$$p'_{44} = \frac{1}{2} (p_{11} - p_{12}) \cos^2(\phi) - p_{14} \sin(\phi) \cos(\phi) + \sin(\phi) (p_{44} \sin(\phi) - p_{41} \cos(\phi)) \quad (\text{S75})$$

$$p'_{45} = \sin(\phi) (p_{41} \sin(\phi) + p_{44} \cos(\phi)) - \cos(\phi) \left(\frac{1}{2} (p_{11} - p_{12}) \sin(\phi) + p_{14} \cos(\phi) \right) \quad (\text{S76})$$

$$p'_{54} = \sin(\phi) \left(p_{14} \sin(\phi) - \frac{1}{2} (p_{11} - p_{12}) \cos(\phi) \right) + \cos(\phi) (p_{44} \sin(\phi) - p_{41} \cos(\phi)) \quad (\text{S77})$$

$$p'_{55} = \sin(\phi) \left(\frac{1}{2} (p_{11} - p_{12}) \sin(\phi) + p_{14} \cos(\phi) \right) + \cos(\phi) (p_{41} \sin(\phi) + p_{44} \cos(\phi)) \quad (\text{S78})$$

$$p'_{61} = \sin(\phi) \left(-p_{41} \sin^3(\phi) + p_{44} \sin(\phi) \sin(2\phi) - p_{13} \cos^3(\phi) + p_{33} \cos^3(\phi) - 2p_{44} \cos^3(\phi) + 2p_{14} \sin(\phi) \cos^2(\phi) \right. \\ \left. + p_{41} \sin(\phi) \cos^2(\phi) - p_{11} \sin^2(\phi) \cos(\phi) + p_{31} \sin^2(\phi) \cos(\phi) \right) \quad (S79)$$

$$p'_{62} = \cos(\phi) \left(p_{33} \sin^3(\phi) + p_{31} \sin(\phi) \cos^2(\phi) + \cos^2(\phi) (2p_{44} \sin(\phi) + p_{41} \cos(\phi)) \right. \\ \left. - \sin(\phi) (p_{11} \cos^2(\phi) + \sin(\phi) (p_{13} \sin(\phi) + 2p_{44} \sin(\phi) + 2p_{14} \cos(\phi) + p_{41} \cos(\phi))) \right) \quad (S80)$$

$$p'_{63} = \frac{1}{2} (p_{12}(-\sin(2\phi)) + p_{31} \sin(2\phi) - 2p_{41} \cos(2\phi)) \quad (S81)$$

$$p'_{66} = \frac{1}{8} \left(2p_{11} \sin^2(2\phi) - 2p_{14} \sin(4\phi) - 2p_{41} \sin(4\phi) + p_{13}(\cos(4\phi) - 1) + p_{31} \cos(4\phi) \right. \\ \left. - p_{33} \cos(4\phi) + 4p_{44} \cos(4\phi) - p_{31} + p_{33} + 4p_{44} \right) \quad (S82)$$

For Y-cut LN, the rotated photoelastic tensor components are given by

$$p'_{\text{LNY}} = \begin{bmatrix} p'_{11} & p'_{12} & p'_{13} & p'_{14} & p'_{15} & p'_{16} \\ p'_{21} & p'_{22} & p'_{23} & p'_{24} & p'_{25} & p'_{26} \\ p'_{31} & p'_{32} & p'_{33} & p'_{34} & p'_{35} & p'_{36} \\ p'_{41} & p'_{42} & p'_{43} & p'_{44} & p'_{45} & p'_{46} \\ p'_{51} & p'_{52} & p'_{53} & p'_{54} & p'_{55} & p'_{56} \\ p'_{61} & p'_{62} & p'_{63} & p'_{64} & p'_{65} & p'_{66} \end{bmatrix}, \quad (S83)$$

where

$$p'_{11} = p_{11} \sin^4(\phi) + p_{44} \sin^2(2\phi) + p_{33} \cos^4(\phi) + p_{13} \sin^2(\phi) \cos^2(\phi) + p_{31} \sin^2(\phi) \cos^2(\phi) \quad (S84)$$

$$p'_{12} = p_{13} \sin^4(\phi) - p_{44} \sin^2(2\phi) + p_{31} \cos^4(\phi) + p_{11} \sin^2(\phi) \cos^2(\phi) + p_{33} \sin^2(\phi) \cos^2(\phi) \quad (S85)$$

$$p'_{13} = p_{12} \sin^2(\phi) + p_{31} \cos^2(\phi) \quad (S86)$$

$$p'_{14} = p_{14} \sin^3(\phi) - 2p_{41} \sin(\phi) \cos^2(\phi) \quad (S87)$$

$$p'_{15} = (p_{14} + 2p_{41}) \sin^2(\phi) \cos(\phi) \quad (S88)$$

$$p'_{16} = \sin(\phi) \cos(\phi) \left(-p_{11} \sin^2(\phi) + p_{13} \sin^2(\phi) - p_{31} \cos^2(\phi) + p_{33} \cos^2(\phi) - 2p_{44} \cos(2\phi) \right) \quad (S89)$$

$$p'_{21} = p_{31} \sin^4(\phi) - p_{44} \sin^2(2\phi) + p_{13} \cos^4(\phi) + p_{11} \sin^2(\phi) \cos^2(\phi) + p_{33} \sin^2(\phi) \cos^2(\phi) \quad (S90)$$

$$p'_{22} = p_{11} \cos^4(\phi) + \sin^2(\phi) \left(p_{33} \sin^2(\phi) + p_{13} \cos^2(\phi) + p_{31} \cos^2(\phi) + 4p_{44} \cos^2(\phi) \right) \quad (S91)$$

$$p'_{23} = p_{31} \sin^2(\phi) + p_{12} \cos^2(\phi) \quad (S92)$$

$$p'_{24} = (p_{14} + 2p_{41}) \sin(\phi) \cos^2(\phi) \quad (S93)$$

$$p'_{25} = p_{14} \cos^3(\phi) - 2p_{41} \sin^2(\phi) \cos(\phi) \quad (S94)$$

$$p'_{26} = \sin(\phi) \cos(\phi) \left(-p_{31} \sin^2(\phi) + p_{33} \sin^2(\phi) - p_{11} \cos^2(\phi) + p_{13} \cos^2(\phi) + 2p_{44} \cos(2\phi) \right) \quad (S95)$$

$$p'_{31} = p_{12} \sin^2(\phi) + p_{13} \cos^2(\phi) \quad (S96)$$

$$p'_{32} = p_{13} \sin^2(\phi) + p_{12} \cos^2(\phi) \quad (S97)$$

$$p'_{33} = p_{11} \quad (S98)$$

$$p'_{34} = p_{14}(-\sin(\phi)) \quad (S99)$$

$$p'_{35} = p_{14}(-\cos(\phi)) \quad (S100)$$

$$p'_{36} = (p_{13} - p_{12}) \sin(\phi) \cos(\phi) \quad (S101)$$

$$p'_{41} = p_{41} \sin^3(\phi) - 2p_{14} \sin(\phi) \cos^2(\phi) \quad (S102)$$

$$p'_{42} = (2p_{14} + p_{41}) \sin(\phi) \cos^2(\phi) \quad (S103)$$

$$p'_{43} = p_{41}(-\sin(\phi)) \quad (S104)$$

$$p'_{44} = p_{44} \sin^2(\phi) + \frac{1}{2} (p_{11} - p_{12}) \cos^2(\phi) \quad (S105)$$

$$p'_{45} = \frac{1}{2} (-p_{11} + p_{12} + 2p_{44}) \sin(\phi) \cos(\phi) \quad (S106)$$

$$p'_{46} = \cos(\phi) \left(p_{14} \cos(2\phi) - p_{41} \sin^2(\phi) \right) \quad (S107)$$

$$p'_{51} = (2p_{14} + p_{41}) \sin^2(\phi) \cos(\phi) \quad (\text{S108})$$

$$p'_{52} = p_{41} \cos^3(\phi) - 2p_{14} \sin^2(\phi) \cos(\phi) \quad (\text{S109})$$

$$p'_{53} = p_{41} (-\cos(\phi)) \quad (\text{S110})$$

$$p'_{54} = \frac{1}{2} (-p_{11} + p_{12} + 2p_{44}) \sin(\phi) \cos(\phi) \quad (\text{S111})$$

$$p'_{55} = \frac{1}{2} (p_{11} - p_{12}) \sin^2(\phi) + p_{44} \cos^2(\phi) \quad (\text{S112})$$

$$p'_{56} = -\sin(\phi) (p_{41} \cos^2(\phi) + p_{14} \cos(2\phi)) \quad (\text{S113})$$

$$p'_{61} = \sin(\phi) \cos(\phi) (-p_{11} \sin^2(\phi) + p_{31} \sin^2(\phi) + 2p_{44} \sin^2(\phi) - p_{13} \cos^2(\phi) + (p_{33} - 2p_{44}) \cos^2(\phi)) \quad (\text{S114})$$

$$p'_{62} = \cos(\phi) (p_{33} \sin^3(\phi) + p_{31} \sin(\phi) \cos^2(\phi) + p_{44} \sin(2\phi) \cos(\phi)) \\ - \sin(\phi) (p_{11} \cos^3(\phi) + (p_{13} + 2p_{44}) \sin^2(\phi) \cos(\phi)) \quad (\text{S115})$$

$$p'_{63} = (p_{31} - p_{12}) \sin(\phi) \cos(\phi) \quad (\text{S116})$$

$$p'_{64} = \cos(\phi) (p_{41} \cos(2\phi) - p_{14} \sin^2(\phi)) \quad (\text{S117})$$

$$p'_{65} = -\sin(\phi) (p_{14} \cos^2(\phi) + p_{41} \cos(2\phi)) \quad (\text{S118})$$

$$p'_{66} = \cos^2(\phi) ((p_{33} - p_{31}) \sin^2(\phi) + p_{44} \cos(2\phi)) - \sin^2(\phi) ((p_{13} - p_{11}) \cos^2(\phi) + p_{44} \cos(2\phi)) \quad (\text{S119})$$